Available online at www.sciencedirect.com
ScienceDirect
C. R. Physique 9 (2008) 570–584
COMPTES RENDUS PHYSIQUE
http://france.elsevier.com/direct/COMREN/

Synchrotron x-rays and condensed matter/Rayonnement X synchrotron et matière condensée

Soft X-ray resonant magnetic scattering of magnetic nanostructures

Gerrit van der Laan

Daresbury Laboratory, Warrington WA4 4AD, United Kingdom

Available online 23 October 2007

Abstract

Soft X-ray resonant magnetic scattering offers a unique element-, site- and valence-specific probe to study magnetic structures on the nanoscopic length scale. This new technique, which combines X-ray scattering with X-ray magnetic circular and linear dichroism, is ideally suited to investigate magnetic superlattices and magnetic domain structures. The theoretical analysis of the polarization dependence to determine the vector magnetization profile is presented. This is illustrated with examples studying the closure domains in self-organising magnetic domain structures, the magnetic order in patterned samples, and the local configuration of magnetic nano-objects using coherent X-rays. ***To cite this article: G. van der Laan, C. R. Physique 9 (2008).***

Résumé

Diffusion magnétique résonnante des rayons X mous dans les nanostructures magnétiques. La diffusion magnétique résonnante des rayons X mous offre une possibilité unique de sonder les structures magnétiques à l'échelle nanoscopique avec une sensibilité à l'élément, au site et à la valence. Cette nouvelle technique, qui combine la diffusion des rayons X avec le dichroïsme magnétique circulaire et linéaire, est idéalement adaptée à l'étude des super-réseaux magnétiques et des structures de domaines magnétiques. Nous présentons l'analyse théorique de l'utilisation de la dépendance en polarisation pour déterminer le profil du vecteur magnétisation. Ceci est illustré par des exemples d'étude des domaines de fermeture dans les structures magnétiques auto-organisées, de l'ordre magnétique dans des échantillons structurés et de la configuration locale de nano-objets à l'aide de rayons X cohérents. ***Pour citer cet article : G. van der Laan, C. R. Physique 9 (2008).***

Keywords: X-ray scattering; Nanostructures; Polarization analysis; Magnetic dichroism; Coherent radiation; Speckle pattern; Magnetic domains

Mots-clés : Diffusion des rayons X ; Nanostructures ; Analyse de polarisation ; Dichroïsme magnétique ; Radiation cohérente ; Figure de speckle ; Domaines magnétiques

1. Introduction

X-ray diffraction provides an indispensable tool for structural characterization of crystalline materials, which relies on the Thomson scattering mechanism, i.e., the interaction between photons and the charge density of the electrons. The sensitivity of X-ray scattering to magnetism has been considered theoretically by Platzman and Tzoar [1] and confirmed experimentally by De Bergevin and Brunel [2] in the 1970s. The so called 'non-resonant magnetic scattering' can be related to the scattering of the electromagnetic wave by the orbital and spin moments of the electrons. There-

E-mail address: g.vanderlaan@dl.ac.uk.

1631-0705/$ – see front matter
doi:10.1016/j.crhy.2007.06.004

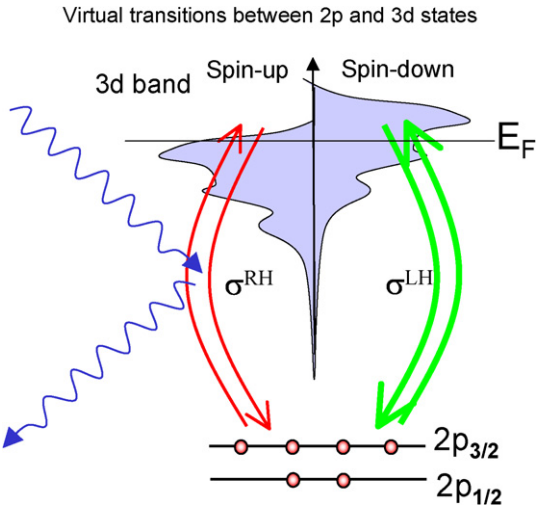

Fig. 1. Schematic picture of the soft X-ray resonant scattering process in a 3d transition metal atom, showing the virtual transitions between the 2p core level and the empty spin-polarized 3d states. The core level is split by the strong spin-orbit interaction, which leads to a difference in the electric-dipole transition probability for left and right circularly polarized X-rays.

fore, the angular dependence of the scattering cross section allows a separation of the spin and orbit contributions to the magnetic moment [3]. The non-resonant magnetic scattering is considerably weaker than the charge scattering and, commonly seen as a curiosity, it lacked the versatility of magnetic scattering by neutrons [4]. However, taking advantage of the tunability of the photon energy of synchrotron radiation in the mid 1980s, two independent discoveries, in X-ray absorption and resonant X-ray scattering, unexpectedly changed this situation for good. The X-ray absorption spectrum showed a huge polarization dependence in the electric dipole allowed transitions of an electron from the core level to the magnetically polarized valence shell, as was predicted theoretically by Thole et al. [5] and confirmed experimentally by van der Laan et al. [6]. Likewise, the elastic process of X-ray absorption followed by emission of a photon in resonant scattering can be regarded as a virtual transition (see Fig. 1). The sensitivity to the magnetization arises from the strong spin-orbit interaction in the core level. A theoretical milestone by Blume [7] was followed by the observation of large polarization dependent resonance effects by Gibbs et al. [8] and Hannon et al. [9] in holmium metal that has served as 'fruit fly' for many experiments. It is important to apprehend that—contrary to the above-mentioned non-resonant scattering—the resonant process is purely due to electric multipole transitions. Twenty years down the line, and stimulated by the large scale access to light sources of synchrotron radiation that are tuneable in energy and polarization, resonant magnetic X-ray scattering has developed into a mature technique for the study of magnetic structures in rare earth, actinide and transition metal compounds. X-ray magnetic scattering measures, like neutron scattering, the spatial Fourier transform of the magnetization, from which one can deduce the spatial distribution of the magnetization in a unit cell and the configuration of the moments, e.g., collinear antiferromagnetic, spiral, cone, etc. However, X-ray resonant magnetic scattering complements neutron scattering because of its element, chemical valence and electron shell specificity, separation of spin and orbital contributions to the magnetic moment, and it can be used in cases where neutron scattering is hampered by small sample size, q-resolution or saturation of the absorption.

For 3d transition metal $L_{2,3}$ edges [10] and rare earth $M_{4,5}$ edges [11] the resonant enhancement largely exceeds the Thomson scattering due to the large radial overlap integral between core and valence electrons. At resonance, the magnetic scattering is comparable in size to the charge scattering. However, for these soft X-ray absorption edges, the wavelength is usually too large for crystalline diffraction, although there are many interesting, and sometimes rather exotic, materials, such as magnetites, perovskites and cuprates, where the elongated unit cell still results in low-order Bragg diffraction peaks. The energy profile of the peak intensity as a function of temperature or/and magnetization can then provide information about spin and orbital ordering, phase transition and Jahn–Teller distortion [12–15].

This article deals with an application of this technique, known as soft X-ray resonant magnetic scattering (SXRMS), to study (pseudo) continuous magnetization distributions in (patterned) magnetic thin films. Even although the wavelength for soft X-rays is longer than the periodicity of the charge and magnetization distributions, it allows us to

Table 1
Extensions to X-ray scattering possible with synchrotron radiation

Extensions to X-ray scattering	Allows one to probe
Tunable X-rays at resonance	Element, site and valence specificity
Polarized X-rays	Magnetic orbital and spin profile
Soft X-rays	Nanoscale sensitivity (down to 1 nm)
Coherent radiation	Local configuration
Pulsed radiation	Dynamics

examine variations on larger length scales. Magnetic nanostructures (defined as 1–100 nm) can show a periodic profile due to artificial patterning or self-assembly, domain structures, or domain closures at the surfaces and interfaces. Therefore, diffraction from such systems offers new possibilities in the field of thin-film magnetism, which has been stimulated by the technological impact of the discovery of technologically important phenomena, such as perpendicular magnetic anisotropy (PMA) and giant magnetoresistance (GMR). SXRMS has the capacity to cover the entire nanometer length scale and is relatively easy to perform on ex-situ prepared samples [16,17]. It has grown into a workhorse technique within the time span of a few years after pioneering experiments by Dürr et al. [18] who measured the circular dichroism of the in-plane diffracted intensity from periodic stripe domains in FePd thin films in reflection geometry. Applications of SXRMS include characterization of structural and magnetic properties of layered and domain systems, especially their interface roughness, induced magnetic order in non-magnetic spacer layer and layer-resolved magnetic moments [19–26]. The tunability of synchrotron radiation allows us to scan the photon energy across the resonance for each of the accessible Bragg peaks. Table 1 shows the extensions to X-ray scattering that have been made possible thanks to synchrotron radiation. Polarization analysis of the scattered beam leads to further characterization of the sample properties [15,27,28]. However, sometimes considered as inconvenient, scattering measurements in the soft X-rays region need to be carried out in a diffractometer that is under vacuum, in order to prevent X-ray absorption by air [16,17,29].

The first part of this article introduces the principles and basic concepts of SXRMS. The suitability of soft X-rays and the probing depth are discussed in Section 2. In Section 3 we get to grips with the formalism of the magnetic scattering cross section and specifically its polarization dependence, which can be used to determine the vector magnetization profile. In the second part of the paper some highlights are presented to illustrate specific applications. Section 4 presents the quintessential magnetic scattering from magnetic stripe domains in FePd alloys, which sheds light on the magnetic domain structure that is governed by the magnetic anisotropy, and it furthermore discusses the micromagnetic modelling of the resonant scattering. Section 5 shows scattering results from artificial structures of Co/Pt nanolines, which give insight in their magnetic order under applied field. Further examples can be found in Refs. [30,31]. Section 6 describes the use of coherent X-rays for scattering with an application to the Co/Pt nanolines to determine the local magnetic configuration. Finally, an outlook is given in Section 7.

2. Suitability of soft X-rays

We concentrate here on the $L_{2,3}$ edges (0.4–1 keV) of the 3d transition metals, which are the most common elements in magnetic materials. Considering the length scale of the periodicities that can be probed by X-ray scattering at a wavelength λ, Bragg's law gives $m\lambda = 2d\sin\theta$, where the integer m is the order of the reflection, the angle θ with the surface plane is the Bragg angle and d is the lattice period. The maximum resolution of $d = \lambda/2$ is obtained at back scattering. As an example, the Fe L_3 edge (707 eV) corresponds to $\lambda = 17.54$ Å, so that $d > 8.8$ Å. For a typical 100 μm slit on an exit arm of 175 mm [29], the angular resolution is equal to $\Delta\theta = 0.033°$, limiting the maximum length of the period that can be measured. This means that at the Fe L_3 a length scale from 1 nm to 1 mm is covered, which is usually too long for crystallography, but ideally suited for the study of magnetic domains, magnetic multilayers, and spin valve structures.

Another important issue is the penetration depth of the soft X-rays, which is determined by the X-ray absorption length that varies strongly across the absorption edge. For Fe metal the absorption length is about 6000 Å just below the L_3 edge, reducing to 170 Å at the top of the L_3 edge and increasing again to 850 Å above the L_2 edge. These values are for the pure metal and the absorption at the L_3 edge scales with the Fe concentration, so that compared to the pure metal the probing depth will be larger in alloys, compounds and dilute systems. Therefore, while absorption

corrections are very important, the probing depth extends over a range of a few thousand Å beneath the surface. This probing depth is much larger than for some common related techniques, such as X-ray absorption using total electron yield and X-ray photoemission. Furthermore, the relatively short X-ray absorption length in resonant scattering can be turned into an advantage, since it allows depth profiling, e.g. to distinguish between buried interfaces at different depths. It will also reduce, or even remove, the contribution from the substrate.

3. Principles of X-ray resonant scattering

3.1. Scattering amplitude

The kinetic energy operator $(\mathbf{p} - e\mathbf{A}/c)^2$ in the photon-matter interaction contains a first-order term in the squared vector potential, $\mathbf{A}^2$, which gives rise to the (non-resonant) Thomson scattering, and a second-order term in $\mathbf{p} \cdot \mathbf{A}$, describing the resonant scattering [32]. The $\mathbf{p} \cdot \mathbf{A}$ term becomes dominant at the resonance energy for excitation of a 2p core electron into an unoccupied 3d valence state. Using the electric-dipole approximation, $\mathbf{A} = \varepsilon \exp(\mathrm{i}\mathbf{k} \cdot \mathbf{r}) \approx \varepsilon$, the matrix element for the coherent amplitude of resonant photon scattering is obtained by the Kramers–Heisenberg formulism as [9,33]

$$\sum_b \langle g|f_b|g\rangle \equiv \sum_b \frac{\langle g|\hat{\varepsilon}'^* \cdot \mathbf{p}|b\rangle\langle b|\mathbf{p} \cdot \hat{\varepsilon}'|g\rangle}{E_b - E_g - \omega - \mathrm{i}\Gamma_b/2} \tag{1}$$

where $\hat{\varepsilon}$ ($\hat{\varepsilon}'$) is the unit polarization vector of the incident (scattered) X-ray beam. The intermediate state b makes the scattering selective to the environment, giving element, site, magnetism, and charge anisotropy sensitivity.

The photon energy ω selects a set of intermediate states b with lifetime Γ_b, assessable from the ground state g. The intermediate state in the resonance process allows additional paths otherwise forbidden in the direct transition, such as spin-flip transitions. The matrix element in Eq. (1) can be written as the expectation value of an effective operator f_n, which after recoupling gives the amplitude for coherent resonant magnetic scattering at the site n, [3,9]

$$f_n(\omega) = f_0(\hat{\varepsilon}'^* \cdot \hat{\varepsilon}) - \mathrm{i}f_1(\hat{\varepsilon}'^* \times \hat{\varepsilon}) \cdot \hat{m}_n + f_2(\hat{\varepsilon}'^* \cdot \hat{m}_n)(\hat{\varepsilon} \cdot \hat{m}_n) \tag{2}$$

where $\hat{m}_n$ is the unit magnetization vector at the nth site, and f_0, f_1 and f_2 are the monopole, magnetic dipole and quadrupole part of the energy dependent resonance amplitude, respectively (f_0 should not be confused with the Fourier transform of the electron density).

The f_0 term gives the anomalous scattering $f_c' + \mathrm{i}f_c''$, which is large near the absorption edge, where it is added to the Thomson scattering. It allows us to observe the charge order. The f_1 term gives the scattering $f_m' + \mathrm{i}f_m''$, which depends linearly on the magnetization direction and can become comparable in size to the f_0 term near specific absorption edges. As an example, Fig. 2 shows the real and imaginary parts of the charge scattering (f_c' and f_c'') and the magnetic scattering (f_m' and f_m'') at the Fe $L_{2,3}$ edges of iron metal. The real and imaginary parts are related to each other by a Kramers–Kronig transform. Thus the resonant amplitudes are complex with strongly energy dependent phase angles. The f_2 term is quadratic in the magnetization direction. Although for completeness we include the f_2 term in Eq. (2), it is usually much smaller than the f_0 and f_1 terms, and it will not be analysed in great detail here, despite the fact that it can give rise to interesting and even controversial effects [34,35].

3.2. Scattering intensity

The magnetic diffraction intensity is a function of both ω and the momentum transfer, given by the scattering vector $\mathbf{q} = \mathbf{k}' - \mathbf{k}$, where $\mathbf{k}(\mathbf{k}')$ is the wave vector of the incident (scattered) X-ray beam. Within the first Born approximation one obtains

$$I(\omega, \mathbf{q}) \propto \left| \sum_n f_n(\omega) \exp(\mathrm{i}\mathbf{q} \cdot \mathbf{r}_n) \right|^2 \tag{3}$$

where the summation is over the sites with position vector $\mathbf{r}_n$.

For a simple collinear structure, with all the magnetization vectors parallel, the polarization dependence of the scattering is the same as for the single site in Eq. (2). This gives an overlap of magnetic and charge peaks, therefore

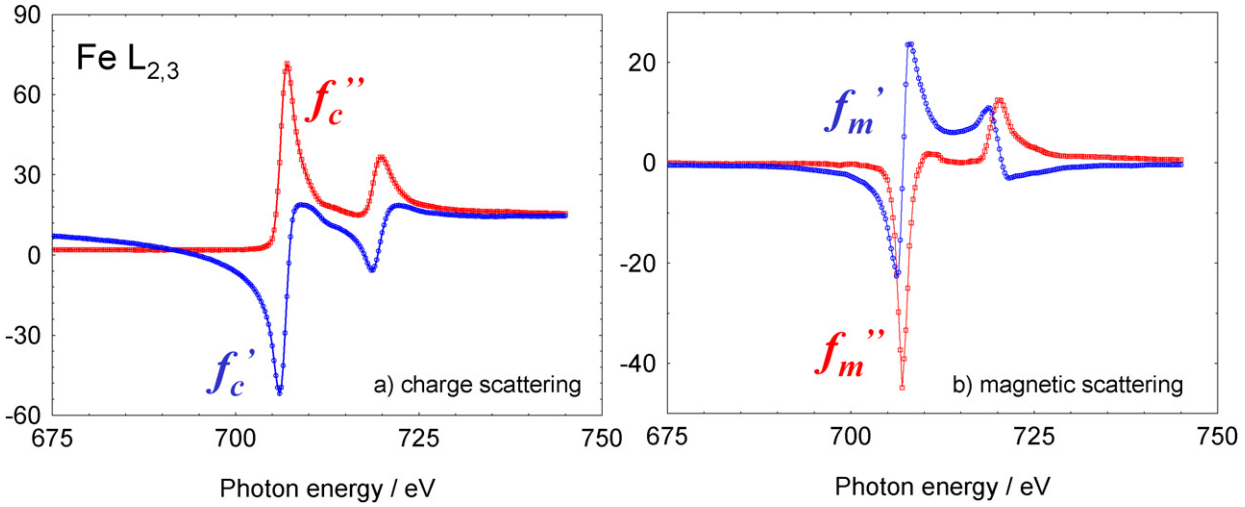

Fig. 2. (a) Real and imaginary part (f_c' and f_c'') of the charge scattering, and (b) real and imaginary part (f_m' and f_m'') of the magnetic scattering at the Fe $L_{2,3}$ edges in iron metal [65].

to study ferromagnetic materials the interference between these two amplitudes has to be used, which shows a change in the scattering signal upon reversal of the sample magnetization. Antiferromagnetically coupled layers or domains offer, like spiral structures, the advantage that the magnetic diffraction peaks are separated from the structural diffraction peaks. Doubling the periodicity in real space gives rise to magnetic peaks with half the structural period in reciprocal space. The distinction between magnetic scattering and Thomson scattering is achieved by tuning on and off the resonance energy.

By taking the $\mathbf{q}$-dependent Fourier transforms F_0, F_1, and F_2 of f_0, f_1, and f_2, respectively, and the Fourier transforms $\bar{\rho}$ and $\widehat{\mathbf{M}}$ of the charge density and the unit magnetization vector, Eq. (2) can be written as

$$F(\mathbf{q}) = F_0\bar{\rho}(\hat{\varepsilon}'^{*}\cdot\hat{\varepsilon}) - \mathrm{i}F_1(\hat{\varepsilon}'^{*}\times\hat{\varepsilon})\cdot\widehat{\mathbf{M}} + F_2(\hat{\varepsilon}'^{*}\cdot\widehat{\mathbf{M}})(\hat{\varepsilon}\cdot\widehat{\mathbf{M}}) \equiv M_c(\mathbf{q}) + M_m(\mathbf{q}) + M_Q(\mathbf{q}) \tag{4}$$

where $M_c(\mathbf{q})$, $M_m(\mathbf{q})$, and $M_Q(\mathbf{q})$ will be used below to refer to the Fourier transforms of the charge, magnetic and quadrupolar contributions, respectively.

3.3. Polarization dependence

We discuss in detail the dependence upon the incidence polarization since it allows to determine the vector magnetization profile. It is convenient to write the geometric part as a 2×2 matrix,

$$\begin{pmatrix} \sigma\to\sigma' & \pi\to\sigma' \\ \sigma\to\pi' & \pi\to\pi' \end{pmatrix}$$

representing the different scattering channels, where the linear polarization perpendicular and parallel to the scattering plane is denoted as σ and π polarization, respectively. The primes refer to the scattered beam. Using the unitary vectors along the incident and scattered beams, $\widehat{\mathbf{k}} = \mathbf{k}/k$ and $\widehat{\mathbf{k}}' = \mathbf{k}'/k'$, respectively, we can define an orthogonal coordinate system $(\widehat{\mathbf{u}}_1, \widehat{\mathbf{u}}_2, \widehat{\mathbf{u}}_3)$ given by

$$\begin{pmatrix} \widehat{\mathbf{u}}_1 \\ \widehat{\mathbf{u}}_3 \end{pmatrix} = \frac{1}{2}\begin{pmatrix} \cos^{-1}\theta & \cos^{-1}\theta \\ \sin^{-1}\theta & -\sin^{-1}\theta \end{pmatrix}\begin{pmatrix} \widehat{\mathbf{k}} \\ \widehat{\mathbf{k}}' \end{pmatrix} \tag{5a}$$

$$\begin{pmatrix} \widehat{\mathbf{k}} \\ \widehat{\mathbf{k}}' \end{pmatrix} = \begin{pmatrix} \cos\theta & \sin\theta \\ \cos\theta & -\sin\theta \end{pmatrix}\begin{pmatrix} \widehat{\mathbf{u}}_1 \\ \widehat{\mathbf{u}}_3 \end{pmatrix} \tag{5b}$$

$$\widehat{\mathbf{k}}'\times\widehat{\mathbf{k}} = -\widehat{\mathbf{u}}_2\sin 2\theta \tag{5c}$$

where θ is the Bragg angle, thus $\hat{\mathbf{k}}' \cdot \hat{\mathbf{k}} = \cos 2\theta$. In the $(\hat{\mathbf{u}}_1, \hat{\mathbf{u}}_2, \hat{\mathbf{u}}_3)$ basis, the components of $\widehat{\mathbf{M}}$ are (z_1, z_2, z_3). Eq. (4) results in the following matrices

$$M_c(\mathbf{q}) = F_0\bar{\rho}(\hat{\varepsilon}'^* \cdot \hat{\varepsilon}) = F_0\bar{\rho}\begin{pmatrix} 1 & 0 \\ 0 & \hat{\mathbf{k}}' \cdot \hat{\mathbf{k}} \end{pmatrix} = F_0\bar{\rho}\begin{pmatrix} 1 & 0 \\ 0 & \cos 2\theta \end{pmatrix} \tag{6}$$

$$\begin{aligned} M_m(\mathbf{q}) &= -\mathrm{i}F_1(\hat{\varepsilon}'^* \times \hat{\varepsilon}) \cdot \widehat{\mathbf{M}} = -\mathrm{i}F_1\begin{pmatrix} 0 & \hat{\mathbf{k}} \cdot \widehat{\mathbf{M}} \\ -\hat{\mathbf{k}}' \cdot \widehat{\mathbf{M}} & (\hat{\mathbf{k}}' \times \hat{\mathbf{k}}) \cdot \widehat{\mathbf{M}} \end{pmatrix} \\ &= -\mathrm{i}F_1\begin{pmatrix} 0 & z_1\cos\theta + z_3\sin\theta \\ -z_1\cos\theta + z_3\sin\theta & -z_2\cos 2\theta \end{pmatrix} \end{aligned} \tag{7}$$

$$M_Q(\mathbf{q}) = F_2(\hat{\varepsilon}'^* \cdot \widehat{\mathbf{M}})(\hat{\varepsilon} \cdot \widehat{\mathbf{M}}) = F_2\begin{pmatrix} z_2^2 & -z_2(z_1\sin\theta - z_3\cos\theta) \\ z_2(z_1\sin\theta + z_3\cos\theta) & -\cos^2\theta(z_1^2\tan^2\theta + z_3^2) \end{pmatrix} \tag{8}$$

The diagonal matrix in Eq. (6) indicates that charge term does not rotate the polarization direction. Consequently, no charge density will be observed in the $\sigma \to \pi'$ or $\pi \to \sigma'$ channels. Eq. (7) shows that the magnetization component parallel to the scattering plane rotates the polarization channel, i.e., $\sigma \to \pi'$ and $\pi \to \sigma'$, while the magnetization component perpendicular to the scattering plane appears in the $\pi \to \pi'$ channel.

We now introduce the density matrix μ, which in Cartesian coordinates can be written as [36]

$$\mu = \frac{1}{2}(P_0\sigma_0 + \mathbf{P} \cdot \sigma) = \frac{1}{2}\begin{pmatrix} P_0 + P_1 & P_2 - \mathrm{i}P_3 \\ P_2 + \mathrm{i}P_3 & P_0 - P_1 \end{pmatrix} = \frac{1}{2}\begin{pmatrix} P_\sigma & P_2 - \mathrm{i}P_3 \\ P_2 + \mathrm{i}P_3 & P_\pi \end{pmatrix} \tag{9}$$

where $\sigma_0 = \left(\begin{smallmatrix} 1 & 0 \\ 0 & 1 \end{smallmatrix}\right)$ is the unit matrix and σ represents the Pauli matrices, $\sigma_1 = \left(\begin{smallmatrix} 1 & 0 \\ 0 & -1 \end{smallmatrix}\right)$, $\sigma_2 = \left(\begin{smallmatrix} 0 & 1 \\ 1 & 0 \end{smallmatrix}\right)$, and $\sigma_3 = \left(\begin{smallmatrix} 0 & -\mathrm{i} \\ \mathrm{i} & 0 \end{smallmatrix}\right)$. $\mathbf{P} = (P_1, P_2, P_3)$ is the Poincaré–Stokes representation of the polarization. The fraction of unpolarized light in synchrotron radiation can be neglected. Defining $P_\sigma = P_0 + P_1$ and $P_\pi = P_0 - P_1$ we can alternatively write μ as at the r.h.s. in Eq. (9). The values for different pure polarization states are shown in Table 2, from which it can be seen that the polarization average is

$$P_0 = \frac{1}{2}(P_\sigma + P_\pi) = \frac{1}{2}(P_{\text{left}} + P_{\text{right}}) = \frac{1}{2}(P_{45^\circ} + P_{135^\circ}) \tag{10}$$

The cross-section $I(\mathbf{q}) = \mathrm{d}\sigma(\mathbf{q})/\mathrm{d}\Omega$ and the polarization $\mathbf{P}'$ after scattering can be calculated using the density matrix formalism [36]

$$P'_\lambda I(\mathbf{q}) = \sum_{\lambda\lambda'} p_\lambda p_{\lambda'} \langle\lambda|F^\dagger|\lambda'\rangle\langle\lambda'|F|\lambda\rangle \tag{11}$$

where p_λ is the probability for the incident polarization λ, and $p_{\lambda'}$ is the probability to detect polarization λ'. The degree of polarization is

$$P = \langle\sigma\rangle = \mathrm{Tr}[\sigma \cdot \mu] \tag{12}$$

Using the density matrices $\mu = \sum_\lambda |\lambda\rangle p_\lambda \langle\lambda|$ for the incident beam and $\mu' = F \cdot \mu \cdot F^\dagger$ for the scattered beam, together with Eq. (11), we can write

$$I(\mathbf{q}) = \mathrm{Tr}[\mu'] = \mathrm{Tr}[F \cdot \mu \cdot F^\dagger] \tag{13}$$

Table 2
Values of the Poincaré vector components for different pure polarization states

	P_0	P_1	P_2	P_3
σ polarization	1	1	0	0
π polarization	1	−1	0	0
Linear polarization at ±45°	1	0	±1	0
Circular polarization	1	0	0	±1
Polarization averaged	1	0	0	0
Linear dichroism	0	1	0	0
Circular dichroism	0	0	0	1

and the polarization after scattering is

$$\mathbf{P}' = \frac{\mathrm{Tr}[\sigma \cdot \mu']}{\mathrm{Tr}[\mu']} \tag{14}$$

where $\mathrm{Tr}[A]$ indicates the trace (i.e., the sum of the diagonal elements) of a matrix A. Using Eq. (13) with Eq. (4) gives the scattering cross-section

$$\begin{aligned} I(\mathbf{q}) &= \mathrm{Tr}[M_c \cdot \mu \cdot M_c^\dagger] + \mathrm{Tr}[M_m \cdot \mu \cdot M_m^\dagger] + \mathrm{Tr}[M_m \cdot \mu \cdot M_c^\dagger - M_c^* \cdot \mu \cdot M_m^\dagger] \\ &\equiv I_c(\mathbf{q}) + I_m(\mathbf{q}) + I_i(\mathbf{q}) \end{aligned} \tag{15}$$

where I_c, I_m, and I_i refer to the $\mathbf{q}$-dependent intensity of the charge scattering, pure magnetic scattering and interference term between charge and magnetic scattering, respectively. Evaluation of Eq. (15) using Eqs. (6)–(9) gives

$$I_c(\mathbf{q}) = \frac{1}{2}|F_0\bar{\rho}|^2\big[P_\sigma + P_\pi|\hat{\mathbf{k}}' \cdot \hat{\mathbf{k}}|^2\big] \tag{16}$$

$$\begin{aligned} I_m(\mathbf{q}) = {} & \frac{1}{2}|F_1|^2 P_\sigma |\hat{\mathbf{k}}' \cdot \widehat{\mathbf{M}}|^2 + \frac{1}{2}|F_1|^2 P_\pi\big[|\hat{\mathbf{k}} \cdot \widehat{\mathbf{M}}|^2 + |(\hat{\mathbf{k}}' \times \hat{\mathbf{k}}) \cdot \widehat{\mathbf{M}}|^2\big] \\ & - |F_1|^2\,\mathrm{Re}\big[(P_2 + \mathrm{i}P_3)(\hat{\mathbf{k}}' \cdot \widehat{\mathbf{M}}^*)(\hat{\mathbf{k}}' \times \hat{\mathbf{k}}) \cdot \widehat{\mathbf{M}}\big] \end{aligned} \tag{17}$$

$$\begin{aligned} I_i(\mathbf{q}) = {} & P_\pi\,\mathrm{Im}\big[F_0^*\bar{\rho}^* F_1\big((\hat{\mathbf{k}}' \times \hat{\mathbf{k}}) \cdot \widehat{\mathbf{M}}\big)(\hat{\mathbf{k}}' \cdot \hat{\mathbf{k}})\big] \\ & + P_2\,\mathrm{Im}\big[F_0^*\bar{\rho}^* F_1\big(\hat{\mathbf{k}} \cdot \widehat{\mathbf{M}} - (\hat{\mathbf{k}}' \cdot \widehat{\mathbf{M}})(\hat{\mathbf{k}}' \cdot \hat{\mathbf{k}})\big)\big] + P_3\,\mathrm{Re}\big[F_0^*\bar{\rho}^* F_1\big(\hat{\mathbf{k}} \cdot \widehat{\mathbf{M}} + (\hat{\mathbf{k}}' \cdot \widehat{\mathbf{M}})(\hat{\mathbf{k}}' \cdot \hat{\mathbf{k}})\big)\big] \end{aligned} \tag{18}$$

3.4. Example of collinear moments

For $\widehat{\mathbf{M}}$ in the scattering plane: $(\hat{\mathbf{k}}' \times \hat{\mathbf{k}}) \cdot \widehat{\mathbf{M}} = 0$, and for $\widehat{\mathbf{M}}$ perpendicular to the scattering plane: $\hat{\mathbf{k}} \cdot \widehat{\mathbf{M}} = \hat{\mathbf{k}}' \cdot \widehat{\mathbf{M}} = 0$. This simplifies the magnetic scattering in Eq. (17) to

$$I_m(M_{q\parallel}) = \frac{1}{2}|F_1|^2\big[P_\sigma|\hat{\mathbf{k}}' \cdot \widehat{\mathbf{M}}|^2 + P_\pi|\hat{\mathbf{k}} \cdot \widehat{\mathbf{M}}|^2\big] \tag{19}$$

$$I_m(M_{q\perp}) = \frac{1}{2}|F_1|^2 P_\pi\big|(\hat{\mathbf{k}}' \times \hat{\mathbf{k}}) \cdot \widehat{\mathbf{M}}\big|^2 \tag{20}$$

This means that σ and/or π polarization is needed to measure collinear moments in the scattering plane and that π polarization is needed to measure out of plane collinear moments.

Likewise, Eq. (18) for interference scattering simplifies to

$$I_i(M_{q\parallel}) = P_2\,\mathrm{Im}\big[F_0^*\bar{\rho}^* F_1\bar{\rho}^*\big(\hat{\mathbf{k}} \cdot \widehat{\mathbf{M}} - (\hat{\mathbf{k}}' \cdot \widehat{\mathbf{M}})(\hat{\mathbf{k}}' \cdot \hat{\mathbf{k}})\big)\big] + P_3\,\mathrm{Re}\big[F_0^*\bar{\rho}^* F_1\big(\hat{\mathbf{k}} \cdot \widehat{\mathbf{M}} + (\hat{\mathbf{k}}' \cdot \widehat{\mathbf{M}})(\hat{\mathbf{k}}' \cdot \hat{\mathbf{k}})\big)\big] \tag{21}$$

$$I_i(M_{q\perp}) = P_\pi\,\mathrm{Im}\big[F_0^*\bar{\rho}^* F_1\big((\hat{\mathbf{k}}' \times \hat{\mathbf{k}}) \cdot \widehat{\mathbf{M}}\big)(\hat{\mathbf{k}}' \cdot \hat{\mathbf{k}})\big] \tag{22}$$

Thus, either skewed linear or circular polarization is needed to measure $M_{q\parallel}$ and π-polarization is needed to measure $M_{q\perp}$.

In forward scattering (FS), where $\hat{\mathbf{k}}' = \hat{\mathbf{k}}$, this reduces further to

$$I_i(M_{q\parallel})_{\mathrm{FS}} = 2P_3\,\mathrm{Re}\big[F_0^*\bar{\rho}^* F_1(\hat{\mathbf{k}} \cdot \widehat{\mathbf{M}})\big] \tag{23}$$

$$I_i(M_{q\perp})_{\mathrm{FS}} = 0 \tag{24}$$

In ferromagnets the charge and magnetic scattering coincide in reciprocal space. To obtain the magnetic scattering one can measure the flipping ratio by reversing either the magnetization or the incident light polarization.

3.5. Example of complex magnetization profile

Substituting $P_0 = P_1 = P_2 = 0$ and $P_3 = 1$ in Eq. (17) gives the circular dichroism in magnetic scattering.

$$I_m(\mathbf{q}) = |F_1|^2\,\mathrm{Im}\big[(\hat{\mathbf{k}}' \cdot \widehat{\mathbf{M}}^*)(\hat{\mathbf{k}}' \times \hat{\mathbf{k}}) \cdot \widehat{\mathbf{M}}\big] \tag{25}$$

As will be illustrated in Section 4.2, this requires a magnetization profile where the components in the two perpendicular planes must be out-of-phase. It is useful in this respect to introduce a complex magnetization vector $\widehat{\mathbf{M}}_{q\pm} \equiv \widehat{\mathbf{M}}_{q\|(k'\times k)} \pm \mathrm{i}\widehat{\mathbf{M}}_{q\|k'}$ for the magnetization profile with real part along $\widehat{\mathbf{k}}' \times \widehat{\mathbf{k}}$ and imaginary part along $\widehat{\mathbf{k}}'$. This is accomplished in a sinusoidal, helical or chiral magnetization pattern [18,37]. Eqs. (13), (14) give in this case the polarization of the scattered beam

$$P'_\sigma = 0 \tag{26}$$

$$P'_\pi = \frac{|F_1|^2\,\mathrm{Im}[(\widehat{\mathbf{k}}' \cdot \widehat{\mathbf{M}}^*)((\widehat{\mathbf{k}}' \times \widehat{\mathbf{k}}) \cdot \widehat{\mathbf{M}})]}{I_m(\mathbf{q})} = 1 \tag{27}$$

which shows that the scattered beam is π polarized [38].

4. Self-organising magnetic patterns in FePd thin films

4.1. Magnetic stripe domain formation and closure domains

Thin films of FePd alloys form self-organising magnetic patterns, where the magnetization breaks up in domains of different directions in order to reduce the stray field energy [39]. The formation of these domains coincides with the creation of domain walls where the magnetization rotates from one direction to the other at the expense of the exchange and anisotropy energies. The results highlighted here refer to thin films grown at the Commissariat à l'énergie atomique (CEA) in Grenoble (France) by depositing ∼40 nm FePd with molecular beam epitaxy (MBE) onto a MgO(001) substrate, and subsequent capping with a 2 nm thick Pd layer to prevent oxidation and contamination [40,41]. Codeposition of Fe and Pd at equi-atomic composition is performed at elevated temperature of the substrate to control the partial chemical ordering [42]. A range of different anisotropies can be obtained by varying the growth conditions. The perpendicular magnetic anisotropy is quantified by the quality factor $Q = K_u/2\pi M_s^2$, where K_u is the perpendicular anisotropy constant and M_s is the saturation magnetization per volume unit. The magnetic configuration depends on both layer thickness and quality factor Q, which strongly depends on the chemical disorder as controlled by the deposition temperature. Layer-by-layer growth at RT results in weak anisotropy ($Q \approx 0.35$). Codeposition at 220 °C gives medium anisotropy ($Q \approx 0.8$) and codeposition at 350 °C gives high anisotropy ($Q \approx 1.5$). Fig. 3(a) shows the magnetic force microscopy (MFM) image of a FePd film with medium anisotropy, with aligned stripes but with the forks and bifurcations. For samples with high anisotropy, the MFM image shows highly disordered stripes. The evolution in the stripe disorder is due to the difference in the processes that create the magnetic walls. When the anisotropy is weak ($Q < 1$) closure domains will lead to a gradual rotation of the magnetization over the period of the stripe, whereas for strong anisotropy ($Q > 1$) the energy of the domain walls is much larger and their creation occurs by nucleation processes in a way that gives rise to the interlaced domains.

Although one could indirectly infer the presence of closure domains from the stripe ordering observed in the MFM image, this technique is not able to resolve the details of the magnetic closure domains. MFM probes the magnetic stray fields above the sample surface, so that the image reveals only the magnetization in up and down direction. SXRMS, however, gives complementary information, such as the in-plane magnetization, depth profile and correlation length. SXRMS is also insensitive to an applied magnetic field, which makes it a suitable technique for hysteresis loop measurements.

4.2. Magnetic circular dichroism in scattering

Fig. 3 shows the SXRMS at the Fe L_3 energy from a FePd alloy sample of medium anisotropy with striped magnetic domain structures (MFM period of 90 nm), as reported by Dürr et al. [18]. The sample was measured with left (solid red line) and right (dotted blue line) circularly polarized X-rays in the geometry with the scattering plane parallel to the magnetic stripes [18,37,43]. The inset shows the experimental geometry, where the detector is scanned horizontally across the diffraction pattern. The magnetic peaks are observed around the central, specularly reflected X-ray beam, at $q_y/2\pi = \pm 0.011$ Å^{-1} confirming the real space period of $\tau = 2\pi/q_y = 90$ nm (y is transverse direction). The magnetic peaks are only observed at photon energies within a few eV of the absorption edge, which confirms their magnetic origin. The magnetic peaks exhibit a strong circular dichroism. This requires a periodic magnetic ordering

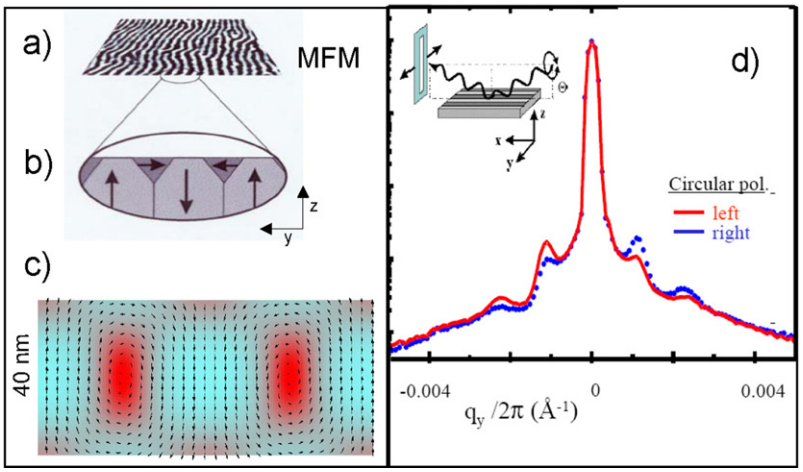

Fig. 3. (a) Magnetic force microscopy (MFM) image of a 2 μm by 2 μm area of a 40 nm thick FePd film grown epitaxially on MgO(001) with striped magnetic domain structures (period of ∼90 nm). The sample has a perpendicular magnetic anisotropy of $Q = 0.8$. The contrast in the MFM image is due to magnetic domains with flux lines directed upward and downward with respect to the film plane. (b) Schematic magnetization profile in the yz plane of the film. The magnetization directions indicated by arrows illustrate the flux closure in the film. (c) Example of a micromagnetic calculation for a unit period of the FePd layer. Each cell (∼1 nm containing ∼10 Fe atoms) is represented by a normalized magnetization vector, shown in the yz plane while the component along the stripe direction is represented by the color gradually increasing from light grey (blue in online version) to dark grey (red in online version). (d) Soft X-ray resonant magnetic scattering (on log scale) at the Fe L_3 edge of a FePd alloy thin film with medium size magnetic anisotropy measured with left (red, drawn line) and right (blue, dotted line) circularly polarized X-rays in a geometry with the scattering plane parallel to the magnetic stripes. The magnetic peaks around the central, specularly reflected X-ray beam show strong magnetic circular dichroism. The left insert shows the experimental geometry with X-rays incident along the stripe direction at grazing angle [18,39,37].

near the surface with a pattern $\uparrow \rightarrow \downarrow \leftarrow$, hence demonstrating the presence of closure domains. A magnetic pattern $\uparrow\downarrow\uparrow\downarrow$ would not give circular dichroism.

The FePd film is structurally homogeneous, hence no interference scattering should be present. Eq. (25) gives the circular dichroism in the magnetic scattering. The circular dichroism requires both a real and imaginary part of the magnetization, which means that the components in the two perpendicular planes must be out-of-phase, i.e., $\widehat{\mathbf{M}}_{q\pm} = \widehat{\mathbf{M}}_{q\|(k'\times k)} \pm \mathrm{i}\widehat{\mathbf{M}}_{q\|k'}$ (cf. Eq. (25)). The first-order satellites are present for both σ and π polarization of the incident beam, but only the out-of-phase interference between the scatterings amplitudes from different domains leads to π' polarization of the outgoing beam, cf. Eq. (27). Thus the phase relation, that is lost for linear polarization, is retrieved with circular polarization. For an 'ideal' ordering ($\uparrow \rightarrow \downarrow \leftarrow \ldots$) with a period of $2\pi/\tau$ we have an ($n = 4$)-fold symmetry axis. The polarized X-rays impose the two phasefactors $\exp(\mathrm{i}\mathbf{q}\cdot\mathbf{r}_j)$ and $\exp(\pm\mathrm{i}\varphi)$ due to the first Born approximation and the elliptical polarization, respectively. For example, the phase factors for right and left circularly polarized light $\hat{\varepsilon}_\pm = (\hat{\varepsilon}_\sigma \pm \mathrm{i}\hat{\varepsilon}_\pi)/\sqrt{2}$ are $\exp(+\mathrm{i}\pi/2)$ and $\exp(-\mathrm{i}\pi/2)$. The phasefactors have to be matched by the sample restrictions $\exp(\mathrm{i}\frac{n}{m}\tau\cdot\mathbf{r}_j)$ and $\exp(\pm\mathrm{i}\frac{n}{m}\varphi)$ due to translation symmetry and rotation symmetry, respectively, where m is an integer. Momentum transfer and angular momentum have to be conserved together, i.e., invariant under simultaneous translation of the unit magnetization vectors by $\pm\frac{2\pi}{\tau}\frac{m}{n}$ and rotation by $\pm 2\pi\frac{m}{n}$. The rotation is clockwise (anticlockwise) for a translation in the positive (negative) direction. Therefore, right and left circularly polarized light give magnetic scattering peaks at $-\tau$ and $+\tau$, respectively.

4.3. Micromagnetic modelling

The microscopic magnetic structure can be calculated by solving numerically the position dependent magnetization vectors using the micromagnetic equations and minimizing the total energy. Using the Gilbert–Landau–Lifshitz (GLL) formulation [44,45], the magnetization is split up in elementary cells (cf. Fig. 3(c)). The total energy contains the Zeeman energy due to external field, the exchange energy, the magnetic anisotropy energy connected with K_u and the demagnetization energy, which depends on the form of the volume magnetization and the saturation magnetization M_s. The energy is minimized under the constraints that the total length of the magnetization vector for each cell

is normalized and that the derivative of the magnetization vanishes perpendicular to the surface. Beutier et al. [46,47] performed numerical simulation of the SXRMS using Eqs. (2), (3), starting from micromagnetic model obtained with the GLL equations which gives the position dependent magnetic moments in the domain pattern. The magnetic profile $\widehat{\mathbf{M}}(\mathbf{q})$ couples with the X-ray polarization vectors to the scalar products $(\widehat{\varepsilon}'^* \times \widehat{\varepsilon}) \cdot \widehat{\mathbf{M}}$ and $(\widehat{\varepsilon}'^* \cdot \widehat{\mathbf{M}})(\widehat{\varepsilon} \cdot \widehat{\mathbf{M}})$.

Dudzik et al. [48] performed depth profiling of the closure domains in FePd by measuring the scattering intensity as a function of Bragg angle. Modeling of the asymmetry ratio of the first- and second-order magnetic peaks as a function of the Bragg angle gave a value of ∼8.5 nm for the effective depth of the closure domains for ∼40 nm FePd films with low to medium anisotropy. This effective depth is in good agreement with the modelled micromagnetic structure and also with the results obtained from a fit of the measured magnetic rod scans [48].

5. Artificial structure of Co/Pt nanolines

Chesnel et al. [49,50] have studied periodic arrays of silicon nanolines, covered by a Co/Pt multilayer, with perpendicular magnetization. SXRMS measurements were used to observe the magnetic order in the perpendicularly magnetized line array. The possibility to tune the photon energy across the Co L_3 edge enables independent measurements of structural order (off-resonance) and magnetic order (at resonance). The scattering is measured in the plane perpendicular to the nanolines. As shown in Fig. 4, the structural diffraction pattern, measured at 760 eV, exhibits many superlattice peaks around the central specular reflection. The peak positions correspond to the structural period of 275 nm and their intensities are modulated by an envelope function due to the form factor given by the shape of the film deposited on the patterned structure. The asymmetry of the spectrum is due to the asymmetry of the sputtering process (the Pt was deposited at 35° oblique incidence angle). Indeed, this asymmetric shape is reversed when the sample is rotated by 180°. At the Co L_3 resonance energy, the magnetic contributions appear both on top of the structural diffraction peaks and between these peaks (Fig. 4). Hence, there will be a strong interference scattering, with the circular dichroism given by Eq. (21) with $P_2 = 0$ and $P_3 = 1$. It vanishes at grazing incidence ($\widehat{\mathbf{k}}' = \widehat{\mathbf{k}}$), since $\widehat{\mathbf{M}}$ is perpendicular to the film.

The magnetic satellites reveal the antiferromagnetic order, which is generated by the interline dipolar coupling. Their intensities depend strongly on the magnetic history, and can be enhanced through specific demagnetisation processes. By applying an in situ magnetic field, the evolution of the magnetic signal can be monitored through the entire hysteresis loop. The magnetic contribution of the structural superlattice peaks can be quantified by their asymmetry ratio, whose angular variation stems from the scattering factor. The change of the intensity with the magnetic field is completely reproducible and characterizes the modifications of the magnetic configuration during the reversal

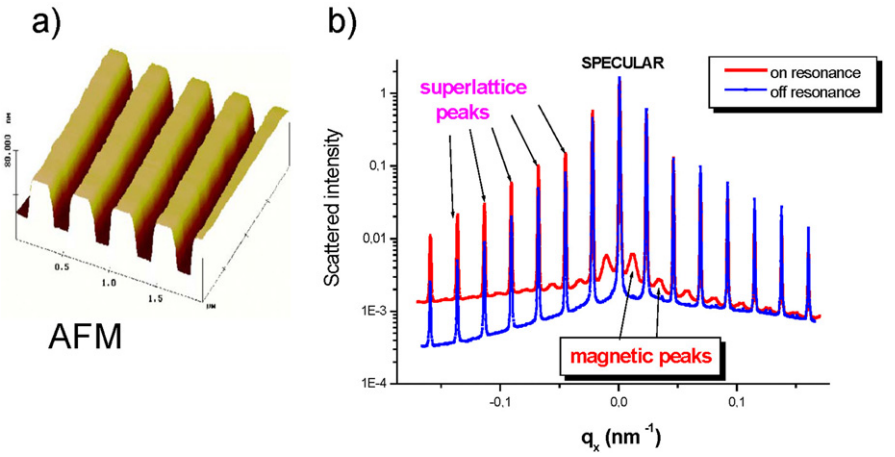

Fig. 4. Periodic array of silicon nanolines, covered by a Co/Pt multilayer, with perpendicular magnetization. (a) Atomic force microscopy (AFM) image of a line grating with linewidth 200 nm, line spacing 200 nm and trench height 35 nm. (b) Normalized diffraction pattern of a line grating with linewidth 200 nm, line spacing 75 nm and trench height 300 nm measured along q_x on the first multilayer Bragg peak ($q_z = 0.24$ Å^{-1}) for two energies: below the Co L_3 edge and at resonance. The magnetic peaks are only observed at resonance [50].

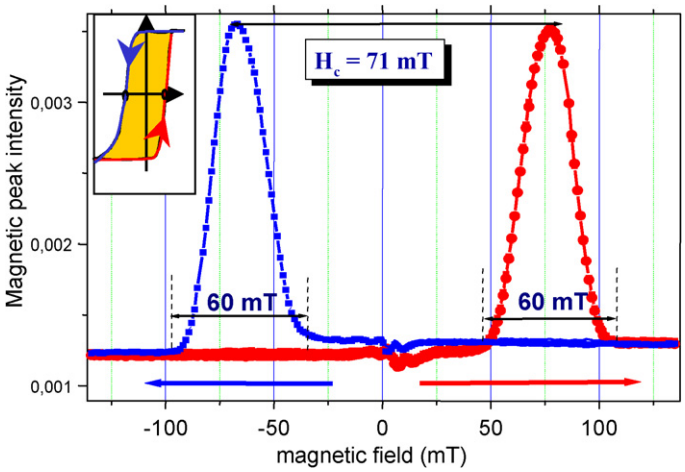

Fig. 5. The antiferromagnetic hysteresis loop of a periodic array of silicon nanolines, covered by a Co/Pt multilayer measured at the magnetic diffraction peaks under in situ perpendicular magnetic field, using XMSR at the Co L_3 resonance. H_c is the coercive field. The inset shows the corresponding hysteresis loop as measured at the super lattice peaks [50].

process. A model of Ising macrospins, developed by Chesnel et al. [50], where the distribution of the magnetic reversal fields is deduced, is in agreement with the measured results.

Applying a perpendicular magnetic field in situ with an electromagnet inside the diffraction chamber [29] enables one to monitor the evolution of the XRMS spectrum with field strength. It is particularly interesting to study the evolution of the magnetic AF satellites and structural peak intensities of different orders when the magnetic field cycles through the hysteresis loop. Fig. 5 shows an example of an antiferromagnetic loop. The signal, monitored by the intensity magnetic peak, is maximum at the coercive point. The main advantage of such measurements is the possibility to follow the signal in real time, with a good time resolution (about 10 Oe/s), compared to MFM studies, which cannot be performed under continuous field variation and which takes longer time.

6. Coherence of X-rays

6.1. Coherence length

Synchrotron radiation, like any other finite source, can be made coherent at the expense of flux, so that a third-generation synchrotron source is required to produce a sufficient coherent flux. The conditions for both longitudinal coherence and transverse coherence have to be fulfilled [51].

The longitudinal (or temporal) coherence length $\xi_l = \lambda^2/(2\Delta\lambda)$ is determined by the resolving power $\lambda/\Delta\lambda$ of the monochromator at given wavelength λ. In the soft X-ray region, $\lambda/\Delta\lambda$ is typically between 1000 and 10 000, so that ξ_l is a few μm. Given that the absorption length μ^{-1} in Fe metal at the L_3 edge is ∼30 nm, the longitudinal coherence condition is largely fulfilled at this resonance.

The transverse (or spatial) coherence is obtained from the diffraction limit as $\xi_t = \lambda z/(2\pi d_s)$, for a distance z from a source with diameter d_s. The required transverse coherence can be achieved by spatial filtering, i.e., by inserting a pinhole with a diameter of typically a few tens of μm at close range in front of the sample [52].

6.2. Speckle pattern

Speckle can be described as the random intensity variation in the scattering of coherent radiation from a random sample. The speckle is caused by the random path differences between the radiation scattered from different locations in the sample, which interfere at the detector in the far field to produce a random interference pattern. Speckle patterns are sensitive to the particular configuration of the random sample, whereas incoherent light scattering is only sensitive to statistical averages of the structure. By measuring the time dependence of the speckle pattern, one can study the dynamics (fluctuation, deformation, etc.) of the system. This would mean that one can study the dynamics of the local

magnetic moments, even when the average sample magnetization is constant. Although the use of coherent visible radiation is well established, only the shorter wavelengths offered by synchrotron radiation will allow us to probe on a shorter length scale than with visible light [53]. Since for X-rays the scattering is small, it is beneficial—using the advantages of synchrotron radiation—to tune into a specific absorption edge, thereby enhancing the scattering and becoming element specific. Polarized radiation gives sensitivity to the magnetization, and to benefit from strong dichroic effects one needs to go to the soft X-ray region.

To reconstruct the local configuration of the illuminated objects from the speckle pattern requires the measurement of the signal $F(\mathbf{u}) = |F(\mathbf{u})|e^{i\phi(\mathbf{u})}$, while only the intensity (i.e., the squared amplitude $|F(\mathbf{u})|^2$) can be detected and the phase $\phi(\mathbf{u})$ is lost. Only under very favourable circumstances, and for a limited number of objects, the phase problem can be solved and the illuminated sample can be reconstructed directly from its coherent scattering pattern [54–57]. Recently, lensless imaging by X-ray spectro-holography of magnetic nanostructures has also been demonstrated [58,59].

The presence of magnetic speckles, displaying a very high magnetic contrast, opens up the possibility to use SXRMS for the study of static and dynamic magnetic disorder on length scales relevant for nanomagnetism. Combined with the time structure of synchrotron radiation, speckle measurements would enable us to study rapid fluctuations in the local magnetic order, giving access to dynamical processes, and ultimately leading to improvements in the read-write speed of magnetic storage devices. This photon in–photon out technique allows us to study reversal processes as a function of magnetic field. It allows us e.g. to determine the degree to which the microscopic domain pattern is retained after magnetization cycling [60,61].

6.3. Coherent SXRMS from Co/Pt nanolines

The use of coherent soft X-rays provides a unique opportunity to go well beyond the incoherent SXRMS results, by following the local reversal mechanism. It has the potential to give access to the local magnetic configuration of the line array, since the area illuminated by the pin hole contains a limited number of nanolines (∼80), so that the spin state of each individual line can be obtained at each stage of the reversal process. The coherent scattering from

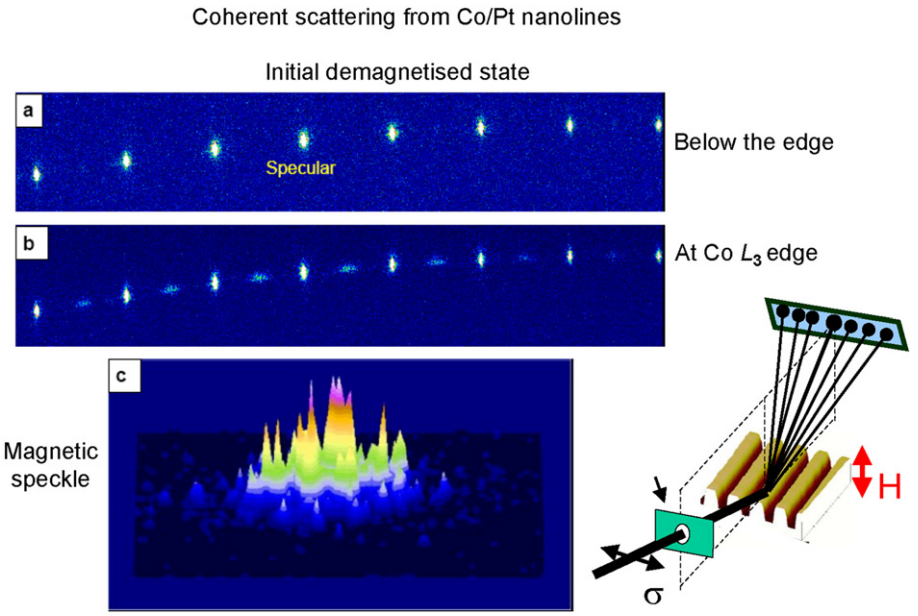

Fig. 6. Coherent scattering from Co/Pt nanolines. (a) The CCD images of the coherent scattering pattern from the patterned sample in the initial demagnetized state, below the absorption edge. (b) At the Co L_3 edge, magnetic satellites appear between the structural diffraction peaks. (c) Three dimensional image of the intensity fluctuations in the first magnetic satellite at the right-hand side of the specular peak. The inset shows a sketch of the experimental set up (not to scale) for coherent scattering in reflection geometry with an incidence angle $\theta = 22.5°$. The scattering pattern is recorded using a charge-coupled device (CCD) camera at $2\theta = 45°$. Each line in the Co/Pt multilayer grating studied here can have either up or down magnetization [60].

the Co/Pt nanolines is shown in Fig. 6. Coherent SXRMS measurements offer the possibility to probe the true local magnetic configuration in nanostructures and its evolution under in situ fields. The remarkable changes of the speckle patterns obtained from a Co/Pt nanoline array along the hysteresis curve provide a precise fingerprint of the evolution of the magnetic domain configuration. The experimental results obtained by Chesnel et al. [60] show that each Co/Pt line behaves like a macrospin that reverses completely above an intrinsic critical field. The whole reversal process of the line assembly can be divided into two regimes: the first stage is a random reversal phase, while the second stage is governed by the dipolar coupling favouring AF ordering. The border between the two regimes depends on the pattern geometry, but also on the intrinsic reversal field distribution and can be modified by various parameters, such as layer deposition mode and magnetic history. Combined with the time structure of synchrotron radiation, these speckle patterns will allow us to study rapid fluctuations in the local magnetic order, giving access to dynamical processes, and ultimately leading to improvements in the read-write speed of magnetic storage devices.

7. Outlook

This brief status report shows that SXRMS opens the way for detailed studies of periodic magnetic nanostructures, which are of high potential interest for spintronics. The scattering technique offers a sufficiently large sampling depth ideal for buried interfaces and can be performed in the presence of externally applied magnetic and electric fields. The element specific magnetization profile is obtained using the linear and circular polarization of the synchrotron radiation. This can not only be used for collinear alignments as in the case of X-ray magnetic circular and linear dichroism, but interestingly also for helical, sinusoidal and chiral magnetization profiles. The presented practical examples of structurally continuous films of FePd with self-organising magnetic stripe patterns and artificial nanostructures covered by a Co/Pt multilayer can be complemented with many other examples, such as the magnetic layer profiles in multilayers [62], systems with modulated magnetic anisotropy [63], and charge, spin and orbital ordering [12], etc. Such studies allow us to obtain direct element-specific information within the structure multilayer or spin valve, e.g., at a buried interface. In the soft X-ray region the magnetic scattering is large, as clearly demonstrated by the presented examples. This brings into reach samples with low concentrations and permits to introduce delta layers to investigate polarization of non-magnetic layers, and makes it possible to verify magnetic dead layers [64].

The use of speckle patterns obtained by coherent X-ray scattering appears to be a very promising development to study magnetic nano-objects. Since soft X-ray absorption spectra show a huge magnetic dichroism compared to their hard X-ray counterparts, the magnetic peak intensities are more straightforward to model. Studies using coherent X-rays clearly hold large promises for the future of magnetic scattering, with imaging of dynamic disorder among the possibilities. Combined with the time structure of synchrotron radiation, speckle measurements will enable us to study rapid fluctuations in the local magnetic order, giving access to dynamical processes, and ultimately leading to improvements in the read-write speed of magnetic storage devices. It also allows us to determine the degree to which the microscopic domain pattern is retained after magnetization cycling.

Acknowledgements

The author gratefully acknowledges the contribution of his collaborators, in particular, M. Belakhovsky, P. Bencok, G. Beutier, N.B. Brookes, K. Chesnel, S.P. Collins, S.S. Dhesi, E. Dudzik, H.A. Dürr, A. Haznar, K. Larsson, F. Livet, A. Marty, M.D. Roper, and N.D. Telling.

References

[1] P. Platzman, N. Tzoar, Phys. Rev. B 2 (1970) 3556.
[2] F. de Bergevin, M. Brunel, Acta Cryst. A 37 (1981) 314.
[3] M. Blume, D. Gibbs, Phys. Rev. B 37 (1988) 1779.
[4] G.L. Squires, Introduction to the Theory of Thermal Neutron Scattering, Cambridge University Press, Cambridge, 1978.
[5] B.T. Thole, G. van der Laan, G.A. Sawatzky, Phys. Rev. Lett. 55 (1985) 2086.
[6] G. van der Laan, B.T. Thole, G.A. Sawatzky, J.B. Goedkoop, J.C. Fuggle, J.M. Esteva, R.C. Karnatak, J.P. Remeika, H.A. Dabkowska, Phys. Rev. B 34 (1986) 6529.
[7] M. Blume, J. Appl. Phys. 57 (1985) 3615.
[8] D. Gibbs, D.R. Harshman, E.D. Isaacs, M.B. McWhan, D. Mills, C. Vettier, Phys. Rev. Lett. 61 (1988) 1241.

[9] J.P. Hannon, G.T. Trammell, M. Blume, D. Gibbs, Phys. Rev. Lett. 61 (1988) 1245;
J.P. Hannon, G.T. Trammell, M. Blume, D. Gibbs, Phys. Rev. Lett. 62 (1989) 2644.
[10] G. van der Laan, B.T. Thole, Phys. Rev. B 43 (1991) 13401.
[11] B.T. Thole, G. van der Laan, J.C. Fuggle, G.A. Sawatzky, R.C. Karnatak, J.M. Esteva, Phys. Rev. B 32 (1985) 5107.
[12] P. Abbamonte, L. Venema, A. Rusydi, G.A. Sawatzky, G. Logvenov, I. Bozovic, Science 297 (2002) 581.
[13] S.S. Dhesi, A. Mirone, C. De Nadai, P. Ohresser, P. Bencok, N.B. Brookes, P. Reutler, A. Revcolevschi, A. Tagliaferri, O. Toulemonde, G. van der Laan, Phys. Rev. Lett. 92 (2004) 056403.
[14] S.B. Wilkins, P.D. Hatton, M.D. Roper, D. Prabhakaran, A.T. Boothroyd, Phys. Rev. Lett. 90 (2003) 187201.
[15] U. Staub, V. Scagnoli, A.M. Mulders, K. Katsumata, Z. Honda, H. Grimmer, M. Horisberger, J.-M. Tonnerre, Phys. Rev. B 71 (2005) 214421.
[16] G. van der Laan, H.A. Dürr, E. Dudzik, M.D. Roper, S.P. Collins, T.P.A. Hase, I. Pape, Synchr. Rad. News 12 (3) (1999) 5.
[17] G. van der Laan, Synchr. Rad. News 14 (5) (2001) 32.
[18] H.A. Dürr, E. Dudzik, S.S. Dhesi, J.B. Goedkoop, G. van der Laan, M. Belakhovsky, C. Mocuta, A. Marty, Y. Samson, Science 284 (1999) 2166.
[19] J.M. Tonnerre, X-ray magnetic scattering in magnetism and synchrotron radiation, in: E. Beaurepaire, B. Carrière, J.P. Kappler (Eds.), Les Ulis, F, Les Editions de Physique, Les Ulis, 1996, pp. 245–274.
[20] T.P.A. Hase, I. Pape, B.K. Tanner, H.A. Dürr, E. Dudzik, G. van der Laan, C.H. Marrows, B.J. Hickey, Phys. Rev. B 61 (2000) R3792.
[21] J.F. MacKay, C. Teichert, D.E. Savage, M.G. Lagally, Phys. Rev. Lett. 77 (1996) 3925.
[22] J.F. MacKay, C. Teichert, M.G. Lagally, J. Appl. Phys. 81 (1997) 4353.
[23] R.M. Osgood, S.K. Sinha, J.W. Freeland, Y.U. Idzerda, S.D. Bader, J. Appl. Phys. 85 (1999) 4619.
[24] J.B. Kortright, S.K. Kim, Phys. Rev. B 62 (2000) 12216.
[25] J.B. Kortright, S.K. Kim, G.P. Denbeaux, G. Zeltzer, K. Takano, E.E. Fullerton, Phys. Rev. B 64 (2001) 092401.
[26] M. Sacchi, C.F. Hague, L. Pasquali, A. Mirone, J.-M. Mariot, P. Isberg, E.M. Gullikson, J.H. Underwood, Phys. Rev. Lett. 81 (1998) 1521.
[27] J.B. Kortright, M. Rice, R. Carr, Phys. Rev. B 51 (1995) 10240.
[28] L. Braicovich, G. van der Laan, A. Tagliaferri, E. Annese, G. Ghiringhelli, N.B. Brookes, Phys. Rev. B 75 (2007) 184408.
[29] M.D. Roper, G. van der Laan, H.A. Dürr, E. Dudzik, S.P. Collins, M.C. Miller, S.P. Thompson, Nucl. Instrum. Methods A 467–468 (2001) 1101.
[30] G. van der Laan, Curr. Opin. Solid State Mater. Sci. 10 (2006) 120.
[31] Y. Zhu, Modern Techniques for Characterizing Magnetic Materials, Springer-Verlag, Berlin, 2005 (Chapter 4).
[32] A useful introduction can be found in M. Altarelli, Lect. Notes in Phys., vol. 697, 2006, p. 201.
[33] P. Carra, B.T. Thole, Rev. Mod. Phys. 66 (1994) 1509.
[34] S.S. Dhesi, H.A. Dürr, M. Münzenberg, W. Felsch, Phys. Rev. Lett. 90 (2003) 117204.
[35] J.E. Lorenzo, N. Jaouen, J.M. Tonnerre, Phys. Rev. Lett. 94 (2005) 039701.
[36] U. Fano, Rev. Mod. Phys. 29 (1957) 74.
[37] G. van der Laan, E. Dudzik, S.P. Collins, S.S. Dhesi, H.A. Dürr, M. Belakhovsky, K. Chesnel, A. Marty, Y. Samson, B. Gilles, Physica B 283 (2000) 171.
[38] H.A. Dürr, E. Dudzik, S.S. Dhesi, J.B. Goedkoop, G. van der Laan, M. Belakhovsky, C. Mocuta, A. Marty, Y. Samson, J. Synchrotron Rad. 7 (2000) 178.
[39] G. van der Laan, K. Chesnel, M. Belakhovsky, A. Marty, F. Livet, S.P. Collins, E. Dudzik, A. Haznar, J.P. Attané, Superlattices and Microstructures 34 (2003) 107.
[40] V. Gehanno, A. Marty, B. Gilles, Phys. Rev. B 55 (1997) 12552.
[41] Y. Samson, A. Marty, R. Hoffmann, V. Gehanno, B. Gilles, J. Appl. Phys. 85 (1999) 4604.
[42] P. Kamp, A. Marty, B. Gilles, R. Hoffmann, S. Marchesini, M. Belakhovsky, C. Boeglin, H.A. Dürr, S.S. Dhesi, G. van der Laan, A. Rogalev, Phys. Rev. B 59 (1999) 1105.
[43] E. Dudzik, S.S. Dhesi, S.P. Collins, H.A. Dürr, G. van der Laan, K. Chesnel, M. Belakhovsky, J. Appl. Phys. 87 (2000) 5469.
[44] A. Hubert, R. Schaeffer, Magnetic Domains: The Analysis of Magnetic Microstructures, Springer-Verlag, Berlin, 1998.
[45] T. Schrefl, J. Fidler, J. Chapman, J. Phys. D 29 (1996) 2352.
[46] G. Beutier, A. Marty, K. Chesnel, M. Belakhovsky, J.C. Toussaint, B. Gilles, G. van der Laan, S.P. Collins, E. Dudzik, Physica B 345 (2004) 143.
[47] G. Beutier, G. van der Laan, K. Chesnel, A. Marty, M. Belakhovsky, S.P. Collins, E. Dudzik, J.-C. Toussaint, B. Gilles, Phys. Rev. B 71 (2005) 184436.
[48] E. Dudzik, S.S. Dhesi, H.A. Dürr, S.P. Collins, M.D. Roper, G. van der Laan, K. Chesnel, M. Belakhovsky, A. Marty, Y. Samson, Phys. Rev. B 62 (2000) 5779.
[49] K. Chesnel, M. Belakhovsky, S. Landis, B. Rodmacq, E. Dudzik, S.P. Collins, S.S. Dhesi, G. van der Laan, IEEE Trans. Magn. 37 (2001) 1661.
[50] K. Chesnel, M. Belakhovsky, S. Landis, J.C. Toussaint, S.P. Collins, G. van der Laan, E. Dudzik, S.S. Dhesi, Phys. Rev. B 66 (2002) 024435.
[51] M. Born, E. Wolf, Principles of Optics, sixth ed., Cambridge University Press, Cambridge, 1997 (Chapter X).
[52] G. Beutier, A. Marty, F. Livet, G. van der Laan, S. Stanescu, P. Bencok, Rev. Sci. Instrum. (2007), in press.
[53] G. van der Laan, Physica B 345 (2004) 137.
[54] F. van der Veen, F. Pfeiffer, J. Phys.: Condens. Matter 16 (2004) 5003.
[55] K. Chesnel, M. Belakhovsky, F. Livet, S.P. Collins, G. van der Laan, S.S. Dhesi, J.P. Attané, A. Marty, Phys. Rev. B 66 (2002) 172404.
[56] S. Eisebitt, M. Lorgen, W. Eberhardt, J. Luning, J. Stohr, C.T. Rettner, O. Hellwig, E.E. Fullerton, G. Denbeaux, Phys. Rev. B 68 (2003) 104419.

[57] F. Livet, Acta Cryst. A 63 (2007) 87.
[58] S. Eisebitt, J. Luning, W.F. Schlotter, M. Lorgen, O. Hellweg, W. Eberhardt, J. Stohr, Nature 432 (2004) 885.
[59] W.F. Schlotter, R. Rick, K. Chen, A. Scherz, J. Stöhr, J. Lüning, S. Eisebitt, Ch. Günther, W. Eberhardt, O. Hellwig, I. McNulty, Appl. Phys. Lett. 89 (2006) 163112.
[60] K. Chesnel, M. Belakhovsky, G. van der Laan, F. Livet, A. Marty, G. Beutier, S.P. Collins, A. Haznar, Phys. Rev. B 70 (2004) 180402.
[61] M.S. Pierce, R.G. Moore, L.B. Sorensen, S.D. Kevan, O. Hellwig, E.E. Fullerton, J.B. Kortright, Phys. Rev. Lett. 90 (2003) 175502.
[62] N. Jaouen, G. van der Laan, T.K. Johal, F. Wilhelm, A. Rogalev, S. Mylonas, L. Ortega, Phys. Rev. B 70 (2004) 094417.
[63] A. Haznar, G. van der Laan, S.P. Collins, C.A.F. Vaz, J.A.C. Bland, S.S. Dhesi, J. Synchrotron Rad. 11 (2004) 254.
[64] J.S. Claydon, Y.B. Xu, M. Tselepi, J.A.C. Bland, G. van der Laan, Phys. Rev. Lett. 93 (2004) 037206.
[65] N.D. Telling, unpublished.